Published in final edited form as:

ACS Nano. 2021 April 27; 15(4): 6562–6572. doi:10.1021/acsnano.0c09732.

Lipophilicity of Cationic Ligands Promotes Irreversible Adsorption of Nanoparticles to Lipid Bilayers

Christian A. Lochbaum[1,‡], **Alex K. Chew**[2,‡], **Xianzhi Zhang**[3], **Vincent Rotello**[3], **Reid C. Van Lehn**[2], **Joel A. Pedersen**[1,4]

[1]Department of Chemistry, University of Wisconsin–Madison, 1101 University Avenue, Madison, Wisconsin 53706, United States

[2]Department of Chemical and Biological Engineering, University of Wisconsin–Madison, Madison, Wisconsin, 53706, United States

[3]Department of Chemistry, University of Massachusetts–Amherst, Amherst, Massachusetts 01003, United States

[4]Departments of Soil Science and Civil & Environmental Engineering, University of Wisconsin–Madison, 1525 Observatory Dive, Madison, Wisconsin 53706, United States

Abstract

A mechanistic understanding of how the surface properties of engineered nanomaterials influence their interactions with cells is essential for designing materials for applications such as bioimaging and drug delivery, as well as for assessing nanomaterial safety. Ligand-coated gold nanoparticles have been widely investigated because their highly tunable surface properties enable investigations into the effect of ligand functionalization on interactions with biological systems. Lipophilic ligands have been linked to adverse biological outcomes through membrane disruption, but the relationship between ligand lipophilicity and membrane interactions is not well understood. Here,

Corresponding Authors: Joel A. Pedersen – Departments of Chemistry, Soil Science, and and Civil & Environmental Engineering University of Wisconsin–Madison, 1101 University Avenue, Madison, Wisconsin 53706, United States; joelpedersen@wisc.edu, **Reid C. Van Lehn** – Department of Chemical and Biological Engineering, University of Wisconsin–Madison, Madison, Wisconsin, 53706, United States; vanlehn@wisc.edu.

Author Contributions

The manuscript was written through contributions of all authors. All authors have given approval to the final version of the manuscript. C.A.L. and A.K.C. contributed equally. C.A.L. performed QCM-D experimentation and analysis. A.K.C performed MD simulations and analysis. X.Z. synthesized and characterized AuNPs and ligands. C.A.L, J.A.P, A.K.C, and R.C.V. discussed and interpreted results. C.A.L. and A.K.C. wrote the manuscript with editing from J.A.P., R.C.V., and V. M. R.

‡Authors contributed equally

Christian A. Lochbaum – Department of Chemistry University of Wisconsin–Madison, 1101 University Avenue, Madison, Wisconsin 53706, United States

Alex K. Chew – Department of Chemical and Biological Engineering, University of Wisconsin–Madison, Madison, Wisconsin, 53706, United States

Xianzhi Zhang – Department of Chemistry, University of Massachusetts–Amherst, Amherst, Massachusetts 01003, United States

Vincent Rotello – Department of Chemistry, University of Massachusetts–Amherst, Amherst, Massachusetts 01003, United States

Supporting Information

Ligand and AuNP synthesis; characterization of AuNPs in water and buffer; calculation of ligand end group lipophilicity; vesicle and SLB formation and characterization; fitting AuNP adsorption to and desorption from SLB; MD workflow for setting up AuNP-bilayer simulations; radial distribution functions of AuNP–water simulations; simulation system sizes; additional details, convergence, sampling time, and snapshots for US calculations; unbiased simulations initiated from US simulations. This material is available free of charge *via* the Internet at http://pubs.acs.org.

The authors declare no competing interests.

we use a library of cationic ligands coated on 2-nm gold nanoparticles to probe the impact of ligand end group lipophilicity on interactions with supported phosphatidylcholine lipid bilayers as a model for cytoplasmic membranes. Nanoparticle adsorption to and desorption from the model membranes were investigated by quartz crystal microbalance with dissipation monitoring. We find that nanoparticle adsorption to model membranes increases with ligand lipophilicity. The effects of ligand structure on gold nanoparticle attachment were further analyzed using atomistic molecular dynamics simulations, which showed that increasing ligand lipophilicity promotes ligand intercalation into the lipid bilayer. Together, the experimental and simulation results could be described by a two-state model that accounts for initial attachment and subsequent conversion to a quasi-irreversibly bound state. We find that only nanoparticles coated with the most lipophilic ligands in our nanoparticle library undergo conversion to the quasi-irreversible state. We propose that initial attachment is governed by interaction between the ligands and phospholipid tail groups, while conversion into the quasi-irreversibly bound state reflects ligand intercalation between phospholipid tail groups and eventual lipid extraction from the bilayer. Systematic variation of ligand lipophilicity enabled us to demonstrate that the lipophilicity of cationic ligands correlates with nanoparticle-bilayer adsorption and suggests that changing the nonpolar ligand R group promotes a mechanism of ligand intercalation into the bilayer associated with irreversible adsorption.

Graphical Abstract

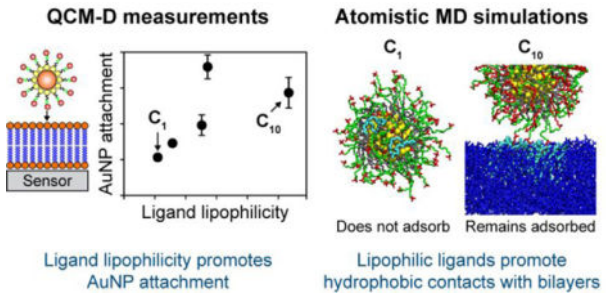

Keywords

nano-bio interface; structure-property relationship; ligand-coated gold nanoparticles; quartz crystal microbalance with dissipation monitoring; supported lipid bilayers; classical molecular dynamics simulations; umbrella sampling

INTRODUCTION

Ligand-coated engineered nanomaterials (ENMs) have been used in bioimaging, drug delivery, and consumer goods, inspiring investigations into understanding how ENMs interact with biological interfaces.[1,2] In particular, establishing relationships between the properties of ENMs and their interactions with cellular membranes is essential for designing safe ENMs.[3,4] For example, interactions between ENMs and cellular membranes can result in lipid extraction[5,6] and membrane disruption,[7,8] events that can lead to cytotoxicity.[7,9,10] However, predicting such behaviors from ligand properties remains challenging, inhibiting ENM design. Toward this end, ligand lipophilicity—the property

quantifying the partitioning of a ligand between aqueous media and lipid, which correlates strongly with hydrophobicity[11]—has been found to dictate ENM interactions with biological interfaces.[12–15] However, the specific interactions between lipophilic ENM ligands and cellular membranes—and the degree to which ligand lipophilicity drives these interactions—remain unclear.

Ligand-coated gold nanoparticles (AuNPs) have been used as model ENMs because of their ease of fabrication and tunable surface chemistry.[16] AuNPs can be synthesized at sizes commensurate with biomolecules (< 10 nm), enabling the study of interactions with biological interfaces at the same length scale.[17] To probe interactions between ENMs and cell membranes, supported lipid bilayers (SLBs) have been used as model membrane systems.[18,19] For example, SLBs have been used to link nanoparticle size, core composition, and surface chemistry to increased cellular interaction, internalization, and cytotoxicity.[7,9] Quartz crystal microbalance with dissipation monitoring (QCM-D) has been used to monitor ENM behavior at the supported lipid bilayer-solution interface through measuring changes in mass and energy dissipation of material coupled to the motion of the sensor.[20] Changes in energy dissipation reflect the viscoelasticity of laterally homogeneous adlayers such as SLBs or to the stiffness of particle–surface contacts.[20,21] QCM-D has been used to deduce mechanisms of peptide incorporation into SLBs,[22] as well as the kinetics of ENM interactions with surfaces.[23,24]

While the kinetics of AuNP adsorption onto SLBs can be quantified *via* QCM-D, other approaches are needed to reveal the molecular-scale AuNP–bilayer interactions that lead to adsorption. As a result, computational models, such as classical molecular dynamics (MD) simulations, have been used to simulate AuNP–bilayer interactions at multiple length scales.[14,25–28] Previous work used atomistic MD simulations to study the free energy of AuNP insertion into the bilayer for AuNPs coated with varying ratios of neutral octanethiol and negatively charged 11-mercapto-1-undecanesulphonate (MUS).[29] Inclusion of more lipophilic ligands (*viz.* octanethiol) lowered the free energy of AuNP insertion into the lipid bilayer, suggesting that AuNP lipophilicity is critical to fusion with the lipid bilayer.[29] Subsequent studies found that AuNP insertion was driven primarily by the lipid membrane core shielding lipophilic ligands from the aqueous environment.[29,30] These studies, in conjunction with related computational results,[14] suggest that the proportion and spatial distribution of lipophilic ligands on AuNP surfaces represent important parameters that modulate potential AuNP insertion into the lipid bilayer. However, the influence of ligand structure, specifically the degree of lipophilicity, on the interaction of AuNPs with lipid membranes remains to be determined.

In this work, we combine QCM-D experiments and atomistic MD simulations to systematically investigate the influence of ligand lipophilicity on AuNP interactions with single-component lipid bilayers. The adsorption of AuNPs to lipid bilayers and their long-term attachment stability increased with ligand lipophilicity. Simulations revealed a mechanism for the long-term stability observed for AuNPs with increased ligand lipophilicity: hydrophobic contacts between ligand lipophilic groups and the lipid tail groups drive the intercalation of more lipophilic ligands into the bilayer or lipid extraction from the bilayer. Kinetic analysis of the QCM-D data accounting for reversible and quasi-irreversible

AuNP adsorption showed agreement with free energy calculations of AuNP–SLB systems. Our findings demonstrate that AuNPs with increased ligand lipophilicity have increased rates of conversion to a quasi-irreversibly bound state, providing design rules for developing ENMs with tailored membrane interactions.

RESULTS AND DISCUSSION

Ligand R Group Lipophilicity Governs AuNP Adsorption to Lipid Bilayers.

Figure 1a shows the library of cationic ligands used to functionalize the 2-nm diameter AuNPs employed in this study. As described in the Methods, ligand lipophilicity is expressed as the equilibrium partition coefficient between phosphatidylcholine liposomes and water ($K_{lip\text{-}w}$) calculated for each ligand R group: methyl (C_1), ethyl (C_2), butyl (C_4), benzyl (Bn), and decyl (C_{10}).[11] Larger log $K_{lip\text{-}w}$ values correspond to a higher propensity for the ligand R group to partition into phosphatidylcholine liposomes from water. By modulating only the ligand R group, we systematically study the effects of R group lipophilicity while keeping the gold core size, charge, and ligand backbone constant. We determined AuNP hydrodynamic diameter and apparent zeta potential by dynamic light scattering and laser Doppler electrophoresis, respectively. Figure S8 shows that in the aqueous solution used for our experiments (10 mM NaCl buffered to pH 7.4 with 10 mM HEPES), the hydrodynamic diameters, and therefore degrees of aggregation, of the AuNPs in our library were comparable. The only statistically significant difference in hydrodynamic diameter was between the Bn- and C_{10}-AuNPs ($p = 0.314$), which we attribute to differences in the polarizability and flexibility of the ligand R groups (*i.e.*, higher polarizability of the benzyl group leading to stronger van der Waals interactions, higher flexibility of the C_{10} R group allowing it to minimize solvent exposure by folding back on itself). The apparent zeta potentials of the AuNPs in our library were statistically indistinguishable and did not differ from zero ($p > 0.05$, Figure S8d; zeta potential mostly between −10 and +10 mV).[31] Given the near neutral apparent zeta potentials of the AuNPs, we do not expect electrostatics to dominate their interaction with bilayers. Similar libraries of AuNPs have been used to correlate cytotoxicity and hydrophobicity.[15]

As described in the Methods, SLBs were prepared from 1,2-dioleoyl-*sn*-glycero-3-phosphocholine (DOPC) using the vesicle fusion method,[32] after which AuNPs (10 nM) were flowed over DOPC lipid bilayers for 20 minutes (schematically represented in Figure 1b) followed by rinsing with AuNP-free solution for extended periods of time. We characterize AuNP-SLB interactions at two distinct time points: after 20 minutes flow —experimentally determined as sufficient time to attain an adsorption plateau—and after extended rinsing. We report QCM-D results as acoustic surface mass density (Γ) and the change in energy dissipation (ΔD). We obtained Γ from frequency changes using the Sauerbrey equation.[20]

Figure 2a shows the acoustic surface mass density for the AuNPs after 20 minutes flow (Γ_{max}) and after rinsing (Γ_{rinse}). We find that C_2−, C_4−, Bn-, and C_{10}-AuNPs adsorb to the DOPC bilayer, whereas any adsorption of C_1-AuNPs was not detectable. For the series of AuNP ligands used, Γ_{max} correlates positively with log $K_{lip\text{-}w}$. For C_2-AuNPs, $\Gamma_{rinse} = 0$, indicating that these AuNPs reversibly adsorb to the lipid bilayer and rinse away using

buffer. In contrast, $\Gamma_{rinse} > 0$ for C_4-, Bn-, and C_{10}-AuNPs, suggesting that a population of these AuNPs remain quasi-irreversibly bound to the bilayer. Given the similarities in particle core size, apparent zeta potential, ligand structure (with the exception of the R group), and hydrodynamic diameter, we expect that the nature of the ligand R group was the dominant contributor to AuNP–bilayer interactions; however, we cannot exclude that aggregation state had a minor influence in the case of the Bn-AuNPs. Increases in AuNP-bilayer interaction with increasing lipophilicity is consistent with established ideas of lipophilic ligand-mediated NP toxicity.[15]

Figure 2b shows change in energy dissipation after 20 minutes flow (ΔD_{max}) and after rinse (ΔD_{rinse}). The C_1-AuNPs do not effect a detectable dissipation change, consistent with the lack of observed mass attachment (Figure 2a). For C_2-AuNPs, zero Γ_{rinse} corresponds with nonzero ΔD_{rinse}. Without a quantifiable population of AuNPs adsorbed to the SLB, either small undetectable populations of AuNPs induce detectable viscoelastic changes to the bilayer, or AuNP adsorption induces a permanent change in the energy dissipation of the bilayer that persists after AuNPs have rinsed away. For C_4-, Bn-, and C_{10}-AuNPs, ΔD_{max} is statistically indistinguishable from ΔD_{rinse} ($p < 0.05$). A population of reversibly adsorbed AuNPs leave the bilayer upon rinsing without producing a detectable change in energy dissipation. From the QCM-D results, we hypothesize that the lipophilicity of C_2-, C_4-, Bn-, and C_{10}-AuNPs leads to spontaneous adsorption onto DOPC lipid bilayers and subsequent formation of a quasi-irreversibly bound state in a subset of the adsorbed AuNP population. Ligand lipophilicity appears to determine the degree of quasi-irreversible interaction, with the least lipophilic ligands leading to negligible quasi-irreversible adsorption. We employ classical molecular dynamics simulations to measure the free energy barriers to forming these states and to gain insight into the mechanism of quasi-irreversibly binding.

Contact between Lipophilic Ligand Groups and Lipid Tails Promotes Adsorption.

We first modeled interactions between C_1- and C_{10}-AuNPs and DOPC lipid bilayers to understand the molecular interactions that drive AuNP adsorption. These AuNPs were selected because the ligands represent the extremes of log $K_{lip\text{-}w}$ in this study and the AuNPs exhibit distinct adsorption behavior: C_1-AuNPs do not adsorb to DOPC bilayers, whereas C_{10}-AuNPs adsorb quasi-irreversibly (Figure 2a). We first quantified potentials of mean force (PMFs) for C_1- and C_{10}-AuNP adsorption using umbrella sampling (US) simulations. The PMF measures the free energy as a function of a collective variable, z, which we define as the distance in the direction normal to the bilayer between the gold core and DOPC center-of-mass (Figure 1c) following past literature.[25–28] We calculated PMFs using initial simulation configurations generated by pulling the AuNP either from an initial position in water toward the bilayer (decreasing-z simulations) or from an initial position in the bilayer toward water (increasing-z simulations). These two methods were used to interrogate potential hysteresis associated with long timescale bilayer rearrangements.[33,34]

Figure 3 compares decreasing-z and increasing-z PMFs for C_1- and C_{10}-AuNPs. Both sets of PMFs are comparable: the decreasing-z PMFs monotonically increase as z decreases, whereas the increasing-z PMFs exhibit free energy minima at positions near the water-

bilayer interface ($z \approx 5$ nm). Simulation snapshots indicate that the free energy minima correspond to configurations in which nonpolar lipid tail groups are in contact with lipophilic groups on the C_1- and C_{10}-AuNPs, suggesting that these favorable contacts lead to thermodynamically preferred adsorbed states for both AuNPs. These minima are consistent with the experimentally observed quasi-irreversibly bound states for C_{10}-AuNPs but do not explain the inability of the C_1-AuNPs to adsorb. However, the pronounced hysteresis between the increasing-z and decreasing-z PMFs suggests that using z as a collective variable does not capture potential free energy barriers that could inhibit adsorption, as previously observed in simulations of lipid insertion into a bilayer.[35]

Unbiased Simulations Reveal Two Mechanisms Leading to Prolonged AuNP Adsorption to Bilayers.

We hypothesized that barriers to the formation of hydrophobic contacts between lipids and the AuNP could explain the differences between the increasing-z and decreasing-z PMFs; previous studies have also identified hydrophobic contacts as important for favorable AuNP-bilayer interactions.[30,36,37] Therefore, we calculated the total number of hydrophobic contacts (c_h) between the alkane and R groups of the ligands and the tail groups of DOPC. Figure 3c plots c_h as a function of z for both increasing-z and decreasing-z simulations. For both AuNPs, many hydrophobic contacts persist during the increasing-z simulations, indicating that hydrophobic contacts are highly favorable. Conversely, hydrophobic contacts are observed for only small values of z during the decreasing-z simulations, indicating the presence of hidden barriers that prevent contacts from forming. To confirm that hydrophobic contacts are important for adsorption, we performed 50-ns unbiased simulations initiated from configurations with different z and c_h values to determine if the C_1- and C_{10}-AuNPs desorb from the bilayer. Figure 4a shows that both C_1- and C_{10}-AuNPs remain adsorbed to the lipid bilayer if the initial value of c_h exceeds ~40 contacts, even for large values of z. These unbiased simulations are consistent with the hypothesis that hydrophobic contacts between the AuNP ligands and lipid membrane are important for adsorption but not captured by z alone.

For unbiased simulations in which the AuNPs remain adsorbed, z increases until $z \approx 5$ nm, thus reaching states consistent with the free energy minima obtained from the increasing-z PMFs. Figure 4b shows final snapshots from the unbiased simulations of C_1- and C_{10}-AuNPs for $z \approx 2$ nm. The snapshots show two mechanisms that promote continued AuNP adsorption: (1) the C_1-AuNP remains adsorbed due to lipid extraction, where lipids are pulled away from the bilayer, and (2) the C_{10}-AuNP remains adsorbed due to both lipid extraction and ligand intercalation, where some C_{10} ligands extend into the hydrophobic core of the bilayer. In both mechanisms, hydrophobic contacts drive the rearrangement of lipids to facilitate AuNP adsorption. C_1 ligands are less capable of facilitating ligand intercalation relative to C_{10} ligands, because the C_1 hydrophobic chain length is shorter than C_{10}.

Ligand Intercalation within Bilayer Reduces Barrier for Forming Hydrophobic Contacts.

The results from the US and unbiased simulations suggest that hydrophobic contacts are important for AuNP adsorption but are not sampled when using z as a collective variable.

We therefore performed US using c_h as a collective variable to calculate a corresponding PMF. We included Bn-AuNP in this analysis, which has intermediate ligand lipophilicity compared to the other ligands and adsorbs quasi-irreversibly (Figure 2a). Figure 5a shows PMFs for C_1-, Bn-, and C_{10}-AuNPs as a function of c_h. The PMF for the C_1-AuNP monotonically increases with c_h, indicating that the initial formation of hydrophobic contacts is unfavorable. The PMF for Bn-AuNP also monotonically increases with larger c_h values, but with a substantially lower slope than C_1-AuNP, which indicates that the more lipophilic Bn ligands reduce the free energy barrier to forming hydrophobic contacts. The PMF for C_{10}-AuNPs has an initial free energy barrier at $c_h = 5$ contacts and a local minimum at $c_h \approx 40$ contacts, then increases monotonically at larger c_h values. The local minimum indicates a metastable state due to the formation of favorable hydrophobic contacts. This metastable state for C_{10}-AuNPs may lead to subsequent ligand intercalation or lipid extraction steps that result in the quasi-irreversibly bound states observed from experiments and the global minimum indicated by the increasing-z PMFs (Figure 3b).

Figure 5b shows simulation snapshots of C_1−, Bn-, and C_{10}-AuNPs for various c_h values. For C_1-AuNPs, ligands contact the bilayer for $c_h \leq 30$ contacts, then a single lipid molecule is extracted for $c_h \geq 40$ contacts. At $c_h = 150$ contacts, the C_1-AuNP desorbs from the DOPC lipid membrane even after extracting two lipid molecules, suggesting that lipid extraction is not sufficiently favorable to promote adsorption without more substantial bilayer deformations (like those observed in Figure 4b). Conversely, the snapshots of the Bn- and C_{10}-AuNPs show that ligands intercalate within the bilayer. For the Bn-AuNP, multiple ligands intercalate within the bilayer with increasing c_h. We attribute the smaller slope of the Bn-AuNP PMF compared to the C_1-AuNP PMF to favorable intercalation. For the C_{10}-AuNP, a single ligand intercalates within the bilayer at $c_h \approx 40$. This value of c_h corresponds to the local minimum in the PMF and is comparable to the threshold for stable adsorption identified from unbiased simulations (Figure 4a). Unlike the Bn-AuNP, multiple C_{10} ligands only intercalate within the bilayer for large values of c_h (≈ 150 contacts). We further tested if ligand intercalation is sufficient to keep the C_{10}-AuNP adsorbed to the DOPC lipid bilayer. We performed four unbiased simulations of each of the three AuNPs initiated with $c_h = 40$ and found that the C_{10}-AuNPs remain adsorbed, whereas most C_1-AuNPs rapidly desorb and Bn-AuNPs desorb but at a slower rate than C_1-AuNPs (Supporting Information, Figure S22).

Taken together, the simulation results suggest that C_1−, Bn- and C_{10}-AuNPs can favorably adsorb to the bilayer if sufficient hydrophobic contacts are formed between the AuNP and the bilayer (Figure 3b). However, C_1-AuNPs can form hydrophobic contacts with the bilayer only *via* a lipid extraction mechanism that is associated with a large free energy barrier (Figure 5). This barrier thus inhibits adsorption in agreement with experimental measurements. Conversely, the more lipophilic R groups present in the Bn and C_{10} ligands intercalate within the bilayer to promote the formation of hydrophobic contacts (Figure 5). Additional snapshots illustrating these two mechanisms are shown in the Supporting Information, Figure S20. Intercalation could facilitate the initial favorable adsorption of Bn- and C_{10}-AuNPs followed by longer timescale interconversion to a quasi-irreversibly adsorbed state associated with many hydrophobic contacts (Figure 2a). Furthermore, ligand

intercalation for C_{10}-AuNPs could explain the experimentally observed bilayer viscoelastic change (Figure 2b).

Two-state Adsorption Kinetics Describes AuNP Reversibly and Quasi-Irreversibly Adsorbed States.

We constructed an analytical kinetic model to investigate the connection between the findings from MD simulations and the experimentally observed quasi-irreversible binding of AuNPs to lipid bilayers. QCM-D cannot directly measure the extent of ligand intercalation, but it does allow two distinct adsorbed states to be distinguished.[23,24,38] We define a three-state model to describe the kinetics of AuNP-SLB interactions which includes a (1) metastable, reversibly adsorbed state, which can undergo either further ligand intercalation, lipid extraction, or desorption; (2) quasi-irreversibly adsorbed state, which corresponds to a high number of hydrophobic contacts consistent with a global free energy minimum (Figure 3b); and (3) desorbed state, which could reflect barriers to forming initial hydrophobic contacts necessary for adsorption.

The two adsorbed states represent a reversibly adsorbed (Γ_α) and a quasi-irreversibly adsorbed (Γ_β) population of nanoparticles. At any given time, the total mass of adsorbed particles equals the sum of the masses of the reversibly and quasi-irreversibly adsorbed particles: $\Gamma_{total}(t) = \Gamma_\alpha(t) + \Gamma_\beta(t)$. Assuming first-order adsorption kinetics, the rate of mass adsorption (the first derivative of mass adsorption with respect to time) can be expressed as a function of the first-order rates of adsorption (k_a), conversion to quasi-irreversibly adsorbed state (k_β), and desorption (k_d). Equation (1) describes the adsorption kinetics, as modified from Zhang *et al.*[23]

$$\frac{d\Gamma_\alpha}{dt} = k_a m_s \frac{\Gamma_{max} - \Gamma_{total}(t)}{\Gamma_{max}} - k_d \theta \Gamma_{total}(t) - k_\beta \theta \Gamma_{total}(t) \quad (1)$$

where m_s is the mass density of AuNPs in solution, and θ is the ratio of reversibly to total adsorbed particles, approximated as $\theta = \frac{\Gamma_{rinse}}{\Gamma_{max}}$. The adsorption capacity of the bilayer was taken as Γ_{max}. Particles that rinse from the bilayer were considered to have been in the reversibly adsorbed α state. Equation (2) describes the desorption of AuNPs from a SLB after AuNPs have been removed from solution.

$$\frac{d\Gamma}{dt} = -k_d \Gamma_{total}(t) \quad (2)$$

To determine the rate coefficient for conversion to the quasi-irreversible adsorption state (k_β), we consider the rate of change of Γ_β independently described by Equation (3).

$$\frac{d\Gamma_\beta}{dt} = k_\beta \theta \Gamma_{total}(t) \quad (3)$$

We have two distinct time points for Γ_β ($t = 0$ min and $t = 20$ min). By integrating over the total time of NP-bilayer exposure ($t_{max} = 20$ min), we determine k_β assuming first-order kinetics:

$$k_\beta = \frac{\Gamma_\beta}{\Gamma_{\text{total}}\theta t} \quad (4)$$

Figure 6 shows the rate coefficients k_a, k_β, and k_d for the different AuNPs. The rate coefficient for adsorption, k_a, increases monotonically with increasing ligand R group lipophilicity as expressed by log $K_{\text{lip–w}}$ (Figure 6a). k_a is dictated by the free energy of binding, which is positively correlated to ligand lipophilicity. The rate coefficient for conversion from the reversible to the quasi-irreversible adsorbed state, k_β, appears to increase with lipophilicity for C_2−, C_4−, Bn- and C_{10}-AuNPs (Figure 6b). After initial adsorption, subsequent ligand intercalation into the bilayer and lipid extraction from the bilayer facilitates the formation of a quasi-irreversibly adsorbed state (Figure 4); therefore, we expect that k_β is dictated by the free energy of hydrophobic contact between ligand R groups and DOPC tail groups. As explored in the MD simulations, increasing ligand R group lipophilicity leads to a decreased free energy barrier for forming hydrophobic contacts (Figure 5). The rate coefficient for desorption of AuNPs in the reversibly adsorbed state, k_d, appears to be independent of ligand R group lipophilicity (Figure 6c), suggesting the mechanism for desorption remains constant between AuNPs of varying ligand lipophilicity. These findings indicate that selection of ligand R group lipophilicity could drive reversible or quasi-irreversible AuNP adsorption onto DOPC bilayers.

CONCLUSIONS

We explored the role of ligand lipophilicity on the adsorption of 2-nm diameter AuNPs to zwitterionic phospholipid bilayers using QCM-D measurements and atomistic MD simulations. The experiments indicated that AuNPs coated with lipophilic ligands can adsorb quasi-irreversibly to DOPC bilayers. The extent of conversion to the quasi-irreversibly adsorbed state scales with ligand functional group lipophilicity. The simulations revealed that AuNP adsorption depends on the number of hydrophobic contacts between the AuNP ligands and the phospholipid acyl chains, which can emerge either due to the intercalation of ligands within the bilayer or the extraction of lipids from the bilayer. Increasing ligand end group lipophilicity promotes intercalation within the bilayer rather than lipid extraction, which reduces the free energy barrier for forming hydrophobic contacts. Analytical modeling of experimental AuNP-bilayer interaction kinetics relates the MD findings to the formation of both reversibly and quasi-irreversibly adsorbed states.

Together, the experiments and simulations suggest a mechanism for AuNP adsorption that depends critically on ligand lipophilicity (Figure 6d). The first step for adsorption is hydrophobic contact between the ligand R group and DOPC tail groups. Since Bn and C_{10} ligands have lipophilic R groups, they can intercalate within the bilayer to promote hydrophobic contacts after overcoming a ~30 kJ·mol^{-1} free energy barrier. At long time scales, Bn- and C_{10}-AuNPs form a quasi-irreversible adsorbed state corresponding to a large number of hydrophobic contacts, consistent with the global free energy minimum in Figure 3b. Conversely, C_1 ligands are unable to make sufficient hydrophobic contacts to maintain adsorption due to the large barrier required for lipid extraction (Figure 5),

resulting in desorption. Our results show that functionalized nanomaterials coated with lipophilic end group ligands could have enhanced adsorption and long-term stability on cell membranes. Tuning nanomaterial ligand lipophilicity may provide a means to enhance targeted nanodrug delivery through selective intercalation of ligands into cell membranes; alternatively, decreasing ligand lipophilicity may allow for creation of environmentally benign nanomaterials.

MATERIALS AND METHODS

Ligand Synthesis.

Figure S1 depicts the synthesis pathway for the ligands used in AuNP functionalization. Compound (1) was synthesized as described by Miranda *et al.*[39] Compound (1) (1.0 g, 2 mmol, 1 eq) was dissolved in 5 mL of ethyl acetate in a 20 mL vial. To each vial, we added 30 eq of the corresponding amine, and the entire solution was sealed properly and heated gently to 50 °C for 3–5 days. Afterward, the solvent was evaporated and the residue was washed three times by hexanes, heptanes, or a 1:1 mixture of hexanes and heptanes to obtain (2) as a yellowish oil-like liquid.

We dissolved 200 mg of (2) in 3 mL of dichloromethane under a nitrogen atmosphere. To the solution we added 20 eq of trifluoroacetic acid followed by addition of 1.2 eq of triisopropylsilane. The solution was stirred at room temperature overnight. Afterward, the solvent was removed, and the residue was washed with hexane or heptane three times and ether for three more times to obtain ligands as colorless or yellowish liquid. To validate the ligand structure, ^{1}H NMR spectroscopy of ligands was performed. Spectra are shown in the Supporting Information, Figures S2–S6.

Gold Nanoparticle Synthesis.

Gold nanoparticles were synthesized by the Brust-Schiffrin two-phase method as described in previous literature.[40,41] In brief, 1 g of $HAuCl_4$ was dissolved in 300 mL 1:1 water toluene. We added 2.1 g of tetraoctylammonium bromide directly with maximum stirring speed. We added 0.7 mL of pentanethiol dropwise until the whole solution turned into white. Then 2.0 g of sodium borohydride was dissolved in around 8 mL of water and immediately added into the white solution. After stirring overnight, the organic layer was separated and dried under reduced pressure in room temperature. The residue was precipitated in cold ethanol and re-dissolved in hexanes. The solution washed with acetonitrile 120 times until all TOAB was fully removed to obtain gold core.

Ligand Exchange Reaction.

Gold cores (40 mg) were dissolved in 4 mL dichloromethane under nitrogen atmosphere. To this solution we added 120 mg of the corresponding ligand in a mixed dichloromethane/methanol (2 mL/2 mL) solution in a dropwise manner under nitrogen and stirred the mixture for 72 h at room temperature. Solvents were removed under reduced pressure, and precipitations were washed with hexanes three times, and hexanes/dichloromethane mixture (1:1 v/v), or pure dichloromethane three times. The solid was suspended in ultrapure water, dialyzed for 3 days, and concentrated by ultracentrifugation. The concentration of gold

nanoparticles was determined based on the absorption at 506 nm as previously reported by Haiss *et al.*[42] Adsorption spectra and compiled absorbance at 506 for all AuNPs are shown in Supporting Information, Figure S7 and Table S1 respectively.

Characterization of AuNP Hydrodynamic and Electrokinetic Properties.

The hydrodynamic diameters and apparent zeta potentials of the AuNPs were determined by dynamic light scattering and laser Doppler electrophoresis, respectively (Malvern Zetasizer Nano ZS). Gold NPs (10 nM) were suspended in water or 10 mM HEPES 10 mM NaCl buffered at pH 7.4 for 30 minutes prior to measurement (Supporting Information, Figure S8). In preliminary experiments, we determined that the AuNPs remained colloidally stable in 10 mM NaCl for the duration of the QCM-D experiments. We therefore selected this salt concentration to study AuNP interaction with bilayers. Higher salt concentrations led to much more pronounced aggregation and destabilized the colloidal suspension.

Calculation of Ligand R group Lipophilicity.

We calculated the lipid–water partition coefficient ($K_{\text{lip-w}}$) of ligand R groups as a measure of ligand lipophilicity using the poly-parameter linear free energy relationship:[11]

$$\log K_{lip-w} = c + eE + sS + aA + bB + vV \tag{5}$$

where E, S, A, B, and V describe the ligand head group excess molar refraction, dipolarity/polarizability, H-bond acidity, H-bond basicity, and molar volume, respectively, and the corresponding lowercase letters are specific for the water–lipid partitioning system.[11] The constant c is obtained from the multiple linear regression used to establish the system descriptors. The chemical descriptors for the ligand R groups (E, S, A, B, and V) were obtained from the Helmholtz Centre for Environmental Research Linear Solvation Energy Relationship.[43] Values for the systems parameters c, e, s, a, b, and v were taken from equation 3 of Endo *et al.*[11] The values for the chemical descriptors and system parameters are compiled in Supporting Information, Table S2.

Vesicle Preparation and SLB Formation.

Solutions for all experiments employing lipids were buffered to pH 7.4 with 10 mM HEPES. Vesicles were formed from 1,2-dioleoyl-*sn*-glycero-3-phosphocholine (DOPC; Avanti Polar Lipids, 850375) *via* vesicle extrusion[44,45]. In short, chloroform was removed from DOPC by evaporation in a vacuum chamber for 1 h. We resuspended DOPC (2.5 mg·mL^{-1}) in 1 mM NaCl. To form vesicles, lipid suspensions were sonicated for 30 min followed by three freeze–thaw cycles (incubation in liquid nitrogen for 5 min followed by sonication at room temperature for 5 min). Vesicles were extruded 11 times through 50 nm polycarbonate filters. The DOPC vesicles had hydrodynamic diameters between 90 and 110 nm as determined by DLS and ζ-potentials of 0 to −6 mV as determined by laser Doppler electrophoresis. Vesicles were stored at 4 °C and used within 10 days.

Supported lipid bilayers were formed on SiO_2-coated QCM-D sensors (QSX203) in a Q-Sense E4 instrument (Biolin Scientific) by vesicle fusion.[20,45] In short, vesicles (0.125 mg·mL^{-1}) in 100 mM NaCl were flowed (0.100 mL·min^{-1}) over sensors freshly cleaned

in an UV/ozone chamber for 20 min. The DOPC vesicles attained a critical surface concentration on the sensors after ~5 min, at which point the vesicles fused and ruptured and a stable bilayer was formed. After signal stabilization, the stable bilayer was rinsed for 10 min with 100 mM NaCl to remove any loosely adhered vesicles. Example frequency and energy dissipation traces for bilayer formation are shown in Supporting Information, Figure S9. The final frequency change for the bilayers was 25 ± 0.5 Hz and the dissipation factor was 0.2 (± 0.1) × 10^{-6}, consistent with values previosuly reported for supported DOPC bilayers.[44]

Nanoparticle Adsorption and Desorption Experiments.

After formation of stable DOPC bilayers on SiO_2-coated QCM-D sensors, we flowed 10 mM NaCl over bilayer until a stable baseline was achieved. We then introduced AuNPs (10 nM) at the same flow rate and in solution of the same composition until a stable plateau in frequency was attained (within 20 min). At this point, AuNP-free solution was introduced into the flow cell and the bilayer was rinsed until a stable baseline was observed. In preliminary experiments with C_{10}-AuNPs, we determined that a AuNP concentration of 10 nM and an exposure time of 20 min was sufficient for a plateau in frequency to be attained. Figure S10 shows changes in acoustic surface mass density and energy dissipation upon exposure of supported lipid bilayers to AuNPs decorated with each of the indicated ligands studied.

We calculated surface mass densities from frequency shifts (Δf_n) using the Sauerbrey equation:[46]

$$\Gamma_{\mathrm{QCMD}} = -C\frac{\Delta f_n}{n} \tag{6}$$

where C is the mass sensitivity constant and n is the harmonic number.[46] Data for AuNP-bilayer interaction were determined to fall within the Sauerbrey regime, $4 \times 10^{-7} Hz^{-1} > > \frac{-\Delta D_n}{\Delta f_{n/n}}$ for a 5 MHz crystal.[20] All data taken between a bilayer baseline and final baseline fit the Sauerbrey regime. For all analysis the 5$^{\mathrm{th}}$ harmonic was used. We calculated the maximum surface mass density, Γ_{max}, at the end of the adsorption phase. We determined $\frac{\mathrm{d}\Gamma}{\mathrm{dt}}$ by taking the derivative of Γ with respect to time: a linear regression algorithm using 33 points (~30 s) centered around one point was used to calculate the derivative. To model the rate coefficients, k_a and k_d, a single-parameter optimized least squares model was used with equations 1 and 2 respectively. Adsorption data were fitted starting from the time the AuNP nanoparticle suspension had displaced AuNP-free solution in the flow chamber (indicated by a positive peak in $\frac{\mathrm{d}\Gamma}{\mathrm{dt}}$) and ending when the AuNP suspension had been displaced from the flow chamber by AuNP-free solution (indicated by a negative peak in $\frac{\mathrm{d}\Gamma}{\mathrm{dt}}$). The time period over which adsorption data were fitted (14 min) corresponds to the duration of AuNP flow minus the time of AuNP addition and removal from the flow cell. Desorption data were fitted for 8 min after observation of the negative peak in $\frac{\mathrm{d}\Gamma}{\mathrm{dt}}$ associated with displacement of the AuNP suspension from the flow chamber.

The results of these fits are shown in Supporting Information, Figure S11 and Figure S12 for adsorption and desorption curves respectively. Goodness of fit was calculated as a non-linear R^2 value and reported in Supporting Information, Table S3.

System Setup for Classical MD Simulations.

Interactions of AuNPs with DOPC bilayers were modeled with classical MD simulations using Gromacs 2016.[47] The simulation workflow for developing the AuNP-DOPC systems is summarized in Supporting Information, Figure S13. AuNPs were modeled using a self-assembly protocol described previously,[48] which outputs 2-nm diameter AuNPs (226 gold atoms) with 83 ligands. AuNPs were modeled by using the INTERFACE force field[49] for gold atoms and the CHARM36/CGenFF force fields[50,51] for the ligands. The AuNPs were solvated with the TIP3P water model[52] with sufficient chlorine counterions to ensure the system is charge-neutral then equilibrated for 5 ns at a temperature T = 300 K (controlled by a velocity-rescale thermostat) and pressure P = 1 bar (controlled by a Berendsen barostat). A 50 ns *NPT* simulation was subsequently performed at the same temperature and pressure, controlled by the same thermostat and Parrinello-Rahman barostat. The last configuration of the 50 ns *NPT* simulation was used to initiate AuNP-DOPC lipid membrane simulations.

The DOPC bilayer was generated using CHARMM36-GUI web-interface[53] with 196 lipids in each of the top and bottom leaflets. The dimensions of the DOPC bilayer were selected to avoid interactions between AuNPs due to the periodic boundary conditions (see Supporting Information, Figure S14). The bilayer was equilibrated with water at T = 300 K with semi-isotropic pressure coupling in the x-y dimensions at P = 1 bar, controlled by Nose-Hoover thermostat and Parinello-Rahman barostat. One AuNP was then inserted into the DOPC system such that the gold core center-of-mass was 6.9 nm away from DOPC center-of-mass and solvated with water (Figure 1c). The AuNP-DOPC lipid membrane system was then equilibrated for 10 ns in the *NPT* ensemble with the AuNP restrained at a 6.9 nm distance from the surface of DOPC with a harmonic potential of 2000 kJ·mol^{-1}·nm^{-2} controlled by the Berendsen thermostat and barostat.

Increasing- and Decreasing-z US Simulations and Subsequent Unbiased Simulations.

We defined z as the center-of-mass distance between the gold core and DOPC bilayer. Initial configurations for the decreasing-z US simulations were generated by pulling the gold core towards the bilayer at 0.0005 nm·ps^{-1} using a harmonic potential with a spring constant of 2000 kJ·mol^{-1}·nm^{-2}. Pulling was performed in the *NPT* ensemble at T = 300 K and P = 1 bar, controlled by the velocity-rescale thermostat and semiisotropic Berendsen barostat. Configurations from this trajectory were used to perform the decreasing-z US simulations with z varying from 1.3 nm to 6.5 nm. Initial configurations for the increasing-z US simulations were generated by pulling the gold core away from the bilayer starting from the final configuration of the z = 1.3 nm window from the decreasing-z US simulations. This pulling simulation used the same harmonic potential and pull rate as the decreasing-z pulling simulations. Configurations from this trajectory were used to perform increasing-z US simulations with z varying from 1.5 to 6.5 nm.

All US simulation windows were equilibrated for 500 ps in the *NPT* ensemble using the velocity-rescale thermostat and Berendsen barostat then simulated for 50 ns using the same thermostat and the Parinello-Rahman barostat. Some windows were extended to an additional 100 ns as discussed in the Supporting Information. The last 40 ns of the production simulation for each window were used to compute the PMF with the Weighted Histogram Analysis Method (WHAM).[54] Additional details on the US protocol and number of simulation windows are provided in the Supporting Information.

Unbiased MD simulations were performed using the 50 ns configuration from either a decreasing- or increasing-z US simulation window. The configuration was equilibrated for 500 ps with the z value restrained using the same spring constant as US simulations. Then, a 50 ns unbiased *NPT* simulation was performed at $P = 1$ bar controlled by the Parinello-Rahman barostat and $T = 300$ K controlled by the velocity-rescale thermostat.

Quantifying the Number of Hydrophobic Contacts.

The total number of hydrophobic contacts (c_h) was defined in Equation 7 by summing all possible contacts between alkane and R group atoms of the ligands (i) and tail group atoms of DOPC (j).

$$c_h = \sum_i \sum_j s_{ij} \tag{7}$$

Equation 8 defines S_{ij} as a continuous function that smoothly decays between 1 (corresponding to a hydrophobic contact) and 0 as a function of distance between atoms i and j (r^{ij}).

$$s_{ij} = \frac{1 - \left(\frac{r_{ij}}{r_o}\right)^6}{1 - \left(\frac{r_{ij}}{r_o}\right)^{12}} \tag{8}$$

r_o is defined as the cutoff when s_{ij} approaches zero and was set to 0.35 nm. Hydrogen atoms were not considered when quantifying the total number of hydrophobic contacts. Hydrophobic contacts were computed using PLUMED Version 2.5.1.[55]

Hydrophobic Contact US Simulations.

We performed US simulations using c_h as the collective variable using PLUMED Version 2.5.1 in conjunction with Gromacs 2016.6. Initial AuNP-DOPC configurations used the last configuration from the decreasing-z US simulations at $z = 5.1$ nm, which has $c_h = 0$ for C_1- and C_{10}-AuNPs (Figure 3c). Initial configurations for US simulations were generated using a *NVT* pulling trajectory with a spring constant of 50 kJ·mol^{-1}·contacts^{-2} (see Supporting Information, Table S7). US simulations were initiated using configurations from the pulling simulations with c_h values between 0 – 150 contacts in increments of 2.5 contacts, totaling up to 61 windows. A spring constant of 10 kJ·mol^{-1}·contacts^{-2} was used for all US simulations. Each simulation window was equilibrated for 500 ps using the velocity-rescale thermostat then simulated for 80 ns using the same thermostat and the

Parinello-Rahman barostat. The last 60 ns of the production simulation for each window were used to compute the PMF with WHAM.[54] For Bn-AuNPs, the last 40 ns of 50 ns production simulations for each window was used to compute the PMF, which was sufficient for convergence (see Supporting Information, Figure S19).

Simulation Parameters.

For all simulations, Verlet lists were generated using a 1.2-nm neighbor list cutoff. van der Waals interactions were modeled with a Lennard-Jones potential using a 1.2-nm cutoff that was smoothly shifted to zero between 1.0 and 1.2 nm. Electrostatic interactions were calculated using the smooth particle mesh Ewald method with a short-range cutoff of 1.2 nm, grid spacing of 0.12 nm, and fourth order interpolation. Bonds were constrained using the LINCS algorithm. Periodic boundary conditions were enabled in all directions.

Supplementary Material

Refer to Web version on PubMed Central for supplementary material.

ACKNOWLEDGEMENTS

This work was supported by the National Science Foundation under grant no. CHE-2001611 and the NSF Center for Sustainable Nanotechnology (CSN). The CSN is part of the Centers for Chemical Innovation Program. X.Z. acknowledges support from the National Institutes of Health (EB0226412) for synthesis and characterization of TCOOH-AuNPs. J.A.P. acknowledges support from a Vilas Distinguished Achievement Professorship and the University of Wisconsin-Madison, Office of the Vice Chancellor for Research and Graduate Education with funding from the Wisconsin Alumni Research Foundation. This work used the Extreme Science and Engineering Discovery Environment (XSEDE), which is supported by National Science Foundation grant number ACI-1548562. We would like to acknowledge Ting Fung Ma (University of Wisconsin-Madison Statistics Department) for helpful discussion on non-linear curve fitting.

REFERENCES

(1). Maurer-Jones MA; Gunsolus IL; Murphy CJ; Haynes CL Toxicity of Engineered Nanoparticles in the Environment. Anal. Chem 2013, 85 (6), 3036–3049. 10.1021/ac303636s. [PubMed: 23427995]

(2). Nel A; Xia T; Mädler L; Li N Toxic Potential of Materials at the Nanolevel. Science. 2006, 311 (5761), 622–627. 10.1126/science.1114397. [PubMed: 16456071]

(3). Hamers RJ Nanomaterials and Global Sustainability. Acc. Chem. Res 2017, 50 (3), 633–637. 10.1021/acs.accounts.6b00634. [PubMed: 28945429]

(4). Johnston LJ; Gonzalez-Rojano N; Wilkinson KJ; Xing B Key Challenges for Evaluation of the Safety of Engineered Nanomaterials. NanoImpact 2020, 18, 100219. 10.1016/j.impact.2020.100219.

(5). Zhu W; von dem Bussche A; Yi X; Qiu Y; Wang Z; Weston P; Hurt RH; Kane AB; Gao H Nanomechanical Mechanism for Lipid Bilayer Damage Induced by Carbon Nanotubes Confined in Intracellular Vesicles. Proc. Natl. Acad. Sci 2016, 113 (44), 12374–12379. 10.1073/pnas.1605030113. [PubMed: 27791073]

(6). Chong G; Foreman-Ortiz IU; Wu M; Bautista A; Murphy CJ; Pedersen JA; Hernandez R Defects in Self-Assembled Monolayers on Nanoparticles Prompt Phospholipid Extraction and Bilayer-Curvature-Dependent Deformations. J. Phys. Chem. C 2019, 123 (45), 27951–27958. 10.1021/acs.jpcc.9b08583.

(7). Bailey CM; Kamaloo E; Waterman KL; Wang KF; Nagarajan R; Camesano TA Size Dependence of Gold Nanoparticle Interactions with a Supported Lipid Bilayer: A QCM-D Study. Biophys. Chem 2015, 203, 51–61. 10.1016/j.bpc.2015.05.006. [PubMed: 26042544]

(8). Liu X; Chen KL Interactions of Graphene Oxide with Model Cell Membranes: Probing Nanoparticle Attachment and Lipid Bilayer Disruption. Langmuir 2015, 31 (44), 12076–12086. 10.1021/acs.langmuir.5b02414. [PubMed: 26466194]

(9). Mensch AC; Hernandez RT; Kuether JE; Torelli MD; Feng ZV; Hamers RJ; Pedersen JA Natural Organic Matter Concentration Impacts the Interaction of Functionalized Diamond Nanoparticles with Model and Actual Bacterial Membranes. Environ. Sci. Technol 2017, 51 (19), 11075–11084. 10.1021/acs.est.7b02823. [PubMed: 28817268]

(10). Olenick LL; Troiano JM; Vartanian A; Melby ES; Mensch AC; Zhang L; Hong J; Mesele O; Qiu T; Bozich J; Lohse S; Zhang X; Kuech T; Millevolte A; Gunsolus I; McGeachy A; Doğangün M; Li T; Hu D; Walter S; et al. Lipid Corona Formation from Nanoparticle Interactions with Bilayers. Chem 2018, 4 (11), 2709–2723. 10.1016/j.chempr.2018.09.018.

(11). Endo S; Escher BI; Goss K-U Capacities of Membrane Lipids to Accumulate Neutral Organic Chemicals. Environ. Sci. Technol 2011, 45 (14), 5912–5921. 10.1021/es200855w. [PubMed: 21671592]

(12). Nel AE; Mädler L; Velegol D; Xia T; Hoek EMV; Somasundaran P; Klaessig F; Castranova V; Thompson M Understanding Biophysicochemical Interactions at the Nano–Bio Interface. Nat. Mater 2009, 8 (7), 543–557. 10.1038/nmat2442. [PubMed: 19525947]

(13). Moyano DF; Goldsmith M; Solfiell DJ; Landesman-Milo D; Miranda OR; Peer D; Rotello VM Nanoparticle Hydrophobicity Dictates Immune Response. J. Am. Chem. Soc 2012, 134 (9), 3965–3967. 10.1021/ja2108905. [PubMed: 22339432]

(14). Rossi G; Monticelli L Gold Nanoparticles in Model Biological Membranes: A Computational Perspective. Biochim. Biophys. Acta - Biomembr 2016, 1858 (10), 2380–2389. 10.1016/j.bbamem.2016.04.001.

(15). Kim ST; Saha K; Kim C; Rotello VM The Role of Surface Functionality in Determining Nanoparticle Cytotoxicity. Acc. Chem. Res 2013, 46 (3), 681–691. 10.1021/ar3000647. [PubMed: 23294365]

(16). Sengani M; Grumezescu AM; Rajeswari VD Recent Trends and Methodologies in Gold Nanoparticle Synthesis – A Prospective Review on Drug Delivery Aspect. OpenNano 2017, 2, 37–46. 10.1016/j.onano.2017.07.001.

(17). You C-C; De M; Rotello VM Monolayer-Protected Nanoparticle-Protein Interactions. Curr. Opin. Chem. Biol 2005, 9 (6), 639–646. 10.1016/j.cbpa.2005.09.012. [PubMed: 16226485]

(18). Troiano JM; Olenick LL; Kuech TR; Melby ES; Hu D; Lohse SE; Mensch AC; Dogangun M; Vartanian AM; Torelli MD; Ehimiaghe E; Walter S; Fu L; Anderton C; Zhu Z; Wang H; Orr G; Murphy C; Hamers R; Pedersen J; Geiger F Direct Probes of 4 Nm Diameter Gold Nanoparticles Interacting with Supported Lipid Bilayers. J. Phys. Chem. C 2015, 119 (1), 534–546. 10.1021/jp512107z.

(19). Melby ES; Lohse SE; Park JE; Vartanian AM; Putans RA; Abbott HB; Hamers RJ; Murphy CJ; Pedersen JA Cascading Effects of Nanoparticle Coatings: Surface Functionalization Dictates the Assemblage of Complexed Proteins and Subsequent Interaction with Model Cell Membranes. ACS Nano 2017, 11 (6), 5489–5499. 10.1021/acsnano.7b00231. [PubMed: 28482159]

(20). Reviakine I; Johannsmann D; Richter RP Hearing What You Cannot See and Visualizing What You Hear: Interpreting Quartz Crystal Microbalance Data from Solvated Interfaces. Anal. Chem 2011, 83 (23), 8838–8848. 10.1021/ac201778h. [PubMed: 21939220]

(21). Yousefi N; Tufenkji N Probing the Interaction between Nanoparticles and Lipid Membranes by Quartz Crystal Microbalance with Dissipation Monitoring. Frontiers in Chemistry 2016, p 46. [PubMed: 27995125]

(22). McCubbin GA; Praporski S; Piantavigna S; Knappe D; Hoffmann R; Bowie JH; Separovic F; Martin LL QCM-D Fingerprinting of Membrane-Active Peptides. Eur. Biophys. J 2011, 40 (4), 437–446. 10.1007/s00249-010-0652-5. [PubMed: 21161523]

(23). Zhang M; Akbulut M Adsorption, Desorption, and Removal of Polymeric Nanomedicine on and from Cellulose Surfaces: Effect of Size. Langmuir 2011, 27 (20), 12550–12559. 10.1021/la202287k. [PubMed: 21879763]

(24). Zhang M; Soto-Rodríguez J; Chen I-C; Akbulut M Adsorption and Removal Dynamics of Polymeric Micellar Nanocarriers Loaded with a Therapeutic Agent on Silica Surfaces. Soft Matter 2013, 9 (42), 10155–10164. 10.1039/C3SM51692J.

(25). Heikkilä E; Martinez-Seara H; Gurtovenko AA; Javanainen M; Häkkinen H; Vattulainen I; Akola J Cationic Au Nanoparticle Binding with Plasma Membrane-Like Lipid Bilayers: Potential Mechanism for Spontaneous Permeation to Cells Revealed by Atomistic Simulations. J. Phys. Chem. C 2014, 118 (20), 11131–11141. 10.1021/jp5024026.

(26). Lolicato F; Joly L; Martinez-Seara H; Fragneto G; Scoppola E; Baldelli Bombelli F; Vattulainen I; Akola J; Maccarini M The Role of Temperature and Lipid Charge on Intake/Uptake of Cationic Gold Nanoparticles into Lipid Bilayers. Small 2019, 15 (23), 1805046. 10.1002/smll.201805046.

(27). Nakamura H; Sezawa K; Hata M; Ohsaki S; Watano S Direct Translocation of Nanoparticles across a Model Cell Membrane by Nanoparticle-Induced Local Enhancement of Membrane Potential. Phys. Chem. Chem. Phys 2019, 21 (35), 18830–18838. 10.1039/C9CP02935D. [PubMed: 31322147]

(28). Lin J; Zhang H; Chen Z; Zheng Y Penetration of Lipid Membranes by Gold Nanoparticles: Insights into Cellular Uptake, Cytotoxicity, and Their Relationship. ACS Nano 2010, 4 (9), 5421–5429. 10.1021/nn1010792. [PubMed: 20799717]

(29). Van Lehn RC; Atukorale PU; Carney RP; Yang Y-S; Stellacci F; Irvine DJ; Alexander-Katz A Effect of Particle Diameter and Surface Composition on the Spontaneous Fusion of Monolayer-Protected Gold Nanoparticles with Lipid Bilayers. Nano Lett 2013, 13 (9), 4060–4067. 10.1021/nl401365n. [PubMed: 23915118]

(30). Simonelli F; Bochicchio D; Ferrando R; Rossi G Monolayer-Protected Anionic Au Nanoparticles Walk into Lipid Membranes Step by Step. J. Phys. Chem. Lett 2015, 6 (16), 3175–3179. 10.1021/acs.jpclett.5b01469.

(31). Clogston JD; Patri AK Zeta Potential Measurement BT - Characterization of Nanoparticles Intended for Drug Delivery; McNeil SE, Ed.; Humana Press: Totowa, NJ, 2011; pp 63–70. 10.1007/978-1-60327-198-1_6.

(32). Melby ES; Mensch AC; Lohse SE; Hu D; Orr G; Murphy CJ; Hamers RJ; Pedersen JA Formation of Supported Lipid Bilayers Containing Phase-Segregated Domains and Their Interaction with Gold Nanoparticles. Environ. Sci. Nano 2016, 3 (1), 45–55. 10.1039/c5en00098j.

(33). Neale C; Bennett WFD; Tieleman DP; Pomès R Statistical Convergence of Equilibrium Properties in Simulations of Molecular Solutes Embedded in Lipid Bilayers. J. Chem. Theory Comput 2011, 7 (12), 4175–4188. 10.1021/ct200316w. [PubMed: 26598360]

(34). Filipe HAL; Moreno MJ; Róg T; Vattulainen I; Loura LMS How to Tackle the Issues in Free Energy Simulations of Long Amphiphiles Interacting with Lipid Membranes: Convergence and Local Membrane Deformations. J. Phys. Chem. B 2014, 118 (13), 3572–3581. 10.1021/jp501622d. [PubMed: 24635540]

(35). Rogers JR; Geissler PL Breakage of Hydrophobic Contacts Limits the Rate of Passive Lipid Exchange between Membranes. J. Phys. Chem. B 2020, 124 (28), 5884–5898. 10.1021/acs.jpcb.0c04139. [PubMed: 32633983]

(36). Van Lehn RC; Ricci M; Silva PHJ; Andreozzi P; Reguera J; Voïtchovsky K; Stellacci F; Alexander-Katz A Lipid Tail Protrusions Mediate the Insertion of Nanoparticles into Model Cell Membranes. Nat. Commun 2014, 5 (1), 4482. 10.1038/ncomms5482. [PubMed: 25042518]

(37). Van Lehn RC; Alexander-Katz A Pathway for Insertion of Amphiphilic Nanoparticles into Defect-Free Lipid Bilayers from Atomistic Molecular Dynamics Simulations. Soft Matter 2015, 11 (16), 3165–3175. 10.1039/C5SM00287G. [PubMed: 25757187]

(38). Van Tassel PR; Viot P; Tarjus G A Kinetic Model of Partially Reversible Protein Adsorption. J. Chem. Phys 1997, 106 (2), 761–770. 10.1063/1.473164.

(39). Miranda OR; Chen H-T; You C-C; Mortenson DE; Yang X-C; Bunz UHF; Rotello VM Enzyme-Amplified Array Sensing of Proteins in Solution and in Biofluids. J. Am. Chem. Soc 2010, 132 (14), 5285–5289. 10.1021/ja1006756. [PubMed: 20329726]

(40). Kanaras AG; Kamounah FS; Schaumburg K; Kiely CJ; Brust M Thioalkylated Tetraethylene Glycol: A New Ligand for Water Soluble Monolayer Protected Gold Clusters. Chem. Commun 2002, No. 20, 2294–2295. 10.1039/B207838B.

(41). Brust M; Walker M; Bethell D; Schiffrin DJ; Whyman R Synthesis of Thiol-Derivatised Gold Nanoparticles in a Two-Phase Liquid–Liquid System. J. Chem. Soc. Chem. Commun 1994, No. 7, 801–802. 10.1039/C39940000801.

(42). Haiss W; Thanh NTK; Aveyard J; Fernig DG Determination of Size and Concentration of Gold Nanoparticles from UV–Vis Spectra. Anal. Chem 2007, 79 (11), 4215–4221. 10.1021/ac0702084. [PubMed: 17458937]

(43). Ulrich S; Brown TN; Watanabe N; Bronner G; Abraham MH; Goss K-U, N. E UFZLSER Database v 3.2 [Internet] Leipzig, Deutschland, Helmholtz Zentrum für Umweltforschung - UFZ 2017.

(44). Cho N-J; Frank CW; Kasemo B; Höök F Quartz Crystal Microbalance with Dissipation Monitoring of Supported Lipid Bilayers on Various Substrates. Nat. Protoc 2010, 5 (6), 1096–1106. 10.1038/nprot.2010.65. [PubMed: 20539285]

(45). Richter RP; Bérat R; Brisson AR Formation of Solid-Supported Lipid Bilayers: An Integrated View. Langmuir 2006, 22 (8), 3497–3505. 10.1021/la052687c. [PubMed: 16584220]

(46). Kankare J Sauerbrey Equation of Quartz Crystal Microbalance in Liquid Medium. Langmuir 2002, 18 (18), 7092–7094. 10.1021/la025911w.

(47). Páll S; Abraham MJ; Kutzner C; Hess B; Lindahl E Tackling Exascale Software Challenges in Molecular Dynamics Simulations with GROMACS BT - Solving Software Challenges for Exascale; Markidis S, Laure E, Eds.; Springer International Publishing: Cham, 2015; pp 3–27.

(48). Chew AK; Van Lehn RC Effect of Core Morphology on the Structural Asymmetry of Alkanethiol Monolayer-Protected Gold Nanoparticles. J. Phys. Chem. C 2018, 122 (45), 26288–26297. 10.1021/acs.jpcc.8b09323.

(49). Heinz H; Vaia RA; Farmer BL; Naik RR Accurate Simulation of Surfaces and Interfaces of Face-Centered Cubic Metals Using 12–6 and 9–6 Lennard-Jones Potentials. J. Phys. Chem. C 2008, 112 (44), 17281–17290. 10.1021/jp801931d.

(50). Best RB; Zhu X; Shim J; Lopes PEM; Mittal J; Feig M; MacKerell AD Optimization of the Additive CHARMM All-Atom Protein Force Field Targeting Improved Sampling of the Backbone ϕ, ψ and Side-Chain X1 and X2 Dihedral Angles. J. Chem. Theory Comput 2012, 8 (9), 3257–3273. 10.1021/ct300400x. [PubMed: 23341755]

(51). Vanommeslaeghe K; Hatcher E; Acharya C; Kundu S; Zhong S; Shim J; Darian E; Guvench O; Lopes P; Vorobyov I; Mackerell A CHARMM General Force Field: A Force Field for Drug-Like Molecules Compatible with the CHARMM All-Atom Additive Biological Force Fields. J. Comput. Chem 2010, 31 (4), 671–690. 10.1002/jcc.21367. [PubMed: 19575467]

(52). Jorgensen WL; Chandrasekhar J; Madura JD; Impey RW; Klein ML Comparison of Simple Potential Functions for Simulating Liquid Water. J. Chem. Phys 1983, 79 (2), 926–935. 10.1063/1.445869.

(53). Jo S; Kim T; Iyer VG; Im W CHARMM-GUI: A Web-Based Graphical User Interface for CHARMM. J. Comput. Chem 2008, 29 (11), 1859–1865. 10.1002/jcc.20945. [PubMed: 18351591]

(54). Kumar S; Rosenberg JM; Bouzida D; Swendsen RH; Kollman PA Multidimensional FreeEnergy Calculations Using the Weighted Histogram Analysis Method. J. Comput. Chem 1995, 16 (11), 1339–1350. 10.1002/jcc.540161104.

(55). Tribello GA; Bonomi M; Branduardi D; Camilloni C; Bussi G PLUMED 2: New Feathers for an Old Bird. Comput. Phys. Commun 2014, 185 (2), 604–613. 10.1016/j.cpc.2013.09.018.

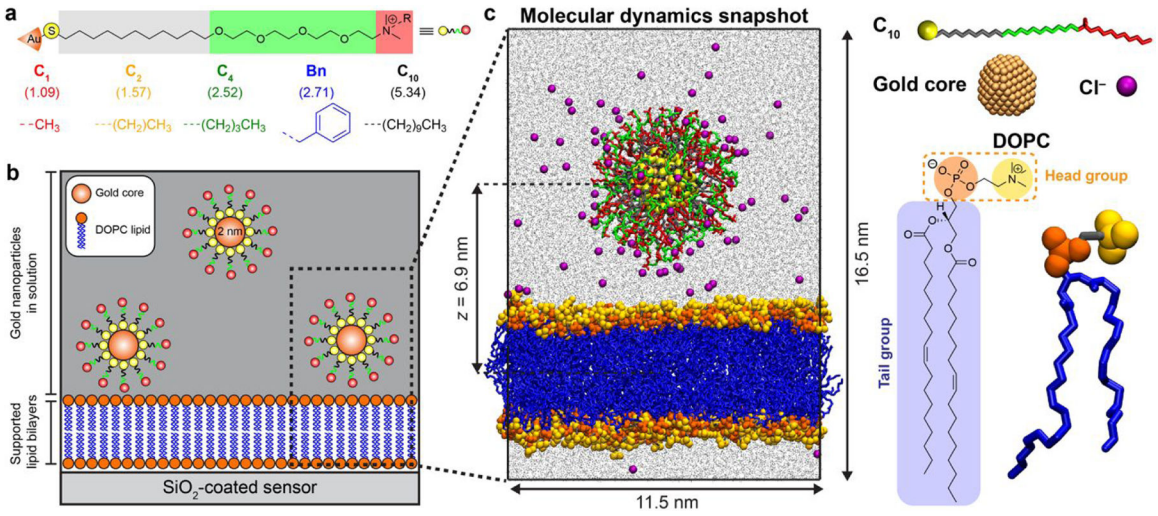

Figure 1.

Experimental and computational systems used to study gold nanoparticle adsorption onto phospholipid bilayers. (a) Ligands are comprised of an alkane group (gray), an oligo(ethylene glycol) spacer group (green), and a cationic quaternary ammonium group (red) substituted with the indicated R group and two methyl groups. The five R groups used are displayed in red and labeled with their calculated log $K_{lip\text{-}w}$ values in parentheses. (b) Schematic of the system used in quartz crystal microbalance experiments to measure nanoparticle adsorption to supported DOPC lipid bilayers. (c) Snapshot of 2-nm gold nanoparticle with C_{10} ligands placed above a DOPC lipid bilayer. The color scheme is illustrated for each of the components at right. The DOPC lipids are comprised of a zwitterionic phosphatidylcholine head group and nonpolar acyl tails consisting primarily of aliphatic carbon atoms. Water is shown in grey.

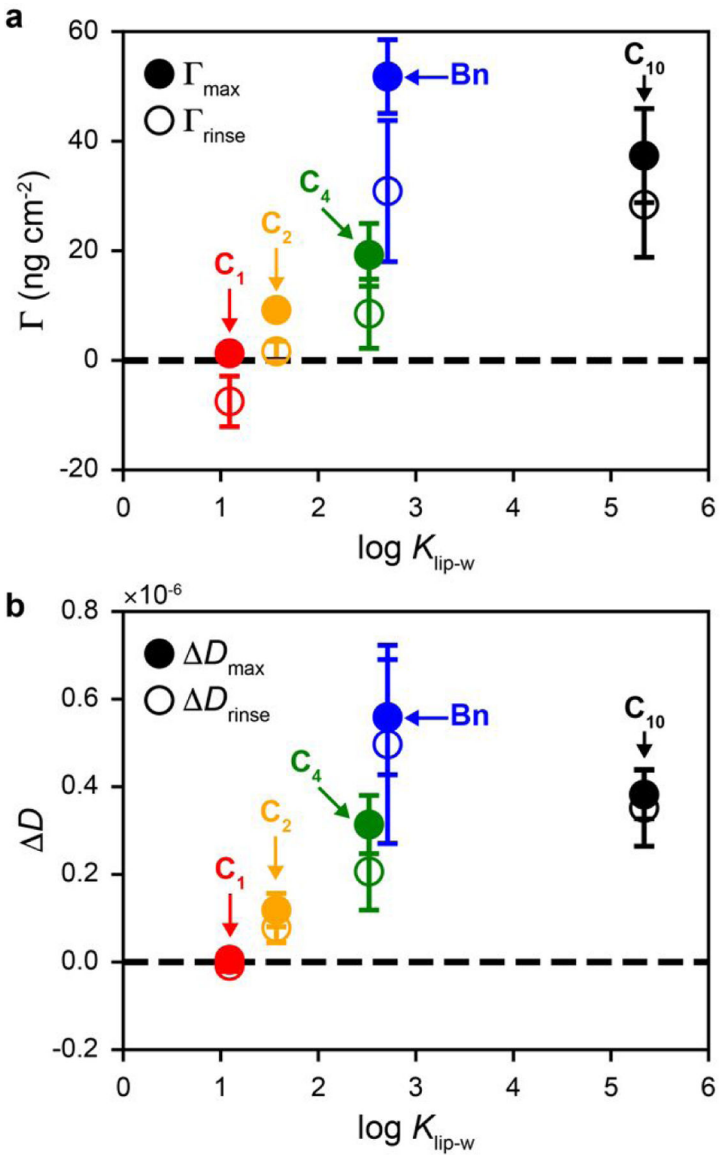

Figure 2.

Influence of ligand lipophilicity on AuNP attachment to supported DOPC bilayers as determined by QCM-D. (a) Acoustic surface mass density (Γ) maximum and after rinse. (b) Dissipation factor (Δ*D*) maximum and after rinse. Error bars represent one standard deviation from four replicate QCM-D experiments.

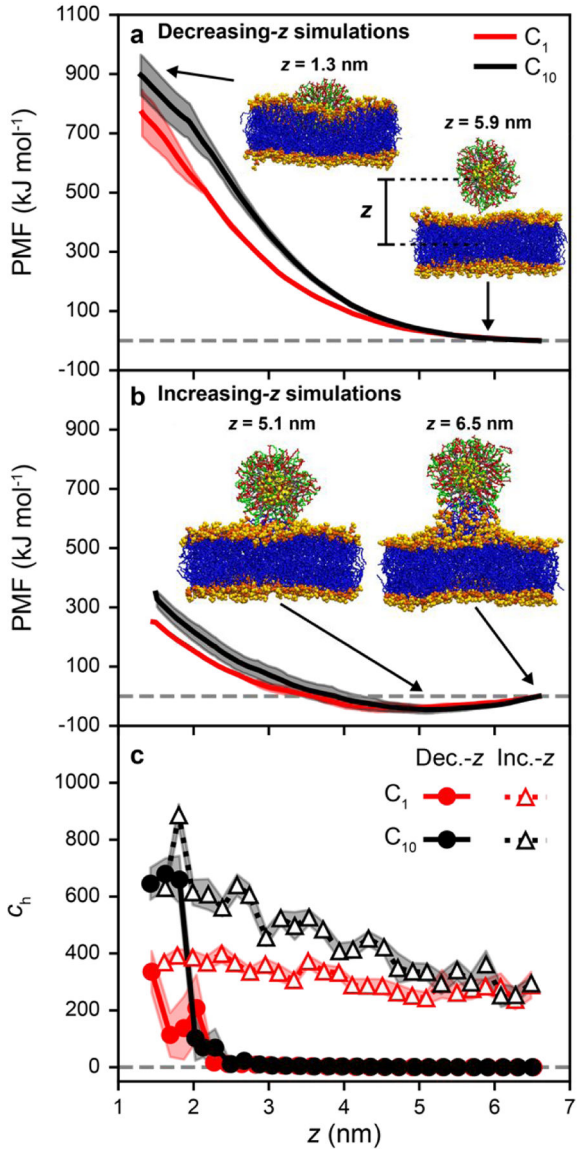

Figure 3.

Free energy as a function of the *z* distance between the AuNP and lipid bilayer. Potential mean force (PMF) *versus z* for C_1− and C_{10}-AuNPs when the gold core is (a) pulled towards (*i.e.* decreasing-z) and (b) away from (*i.e.* increasing-z) the DOPC lipid bilayer. Simulation snapshots show the last configuration from umbrella sampling simulations of C_{10}-AuNPs for different values of *z*. Water and chlorine atoms are omitted for clarity. Legends are the same for (a) and (b). (c) Number of hydrophobic contacts (c_h) *versus z* for both decreasing- and increasing-*z* simulations. Hydrophobic contacts are defined as the number of contacts between nonpolar groups in the ligands and in the DOPC tail groups. Error bars are reported as the standard deviation between two 20 ns blocks for each umbrella sampling window.

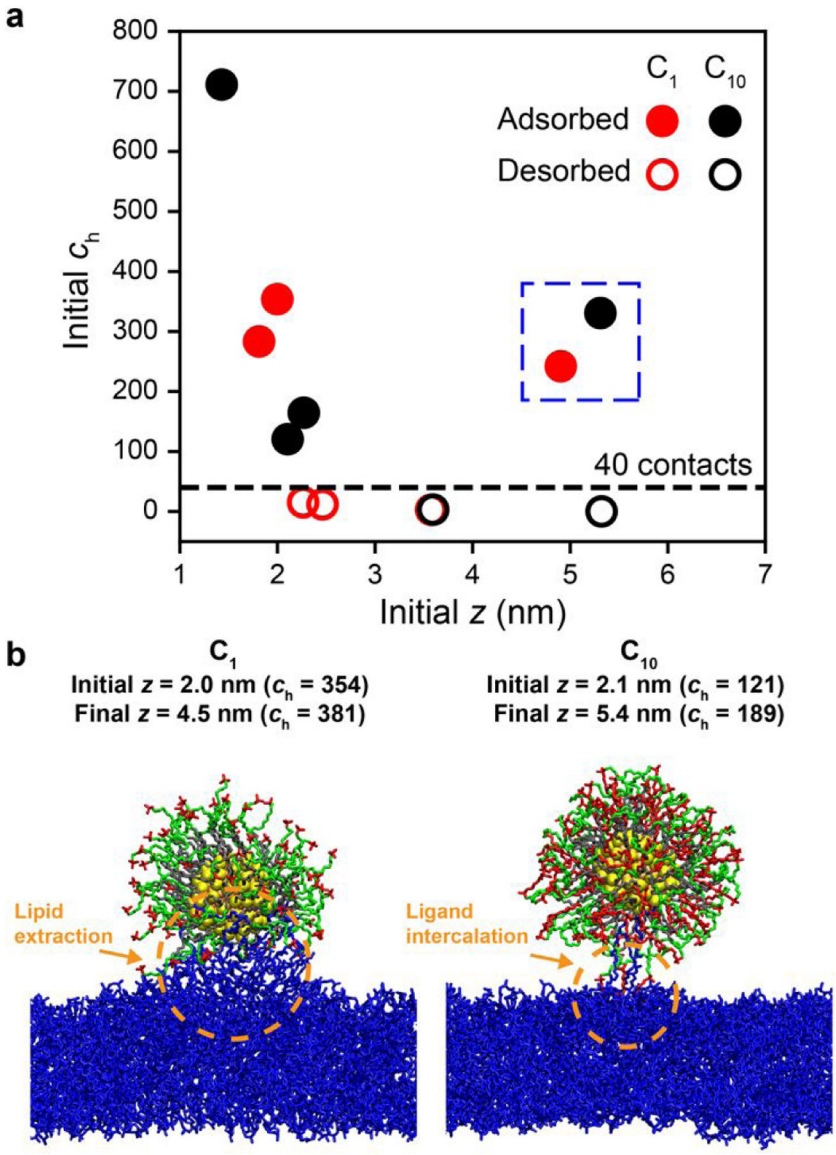

Figure 4.

Unbiased simulations initiated from umbrella sampling trajectories. (a) Number of hydrophobic contacts (c_h) *versus* z for unbiased simulations initiated from increasing- and decreasing-z US configurations for C_1− and C_{10}-AuNPs. AuNPs are considered adsorbed if $z < 6$ nm for the last 10 ns of the unbiased simulation (filled markers) and desorbed if $z > 6$ nm (hollow markers). Points in the dashed blue box were for unbiased simulations initiated from increasing-z US configuration, all other points were for simulations initiated from decreasing-z US configurations. (b) Simulation snapshots after 50 ns of unbiased simulation for C_1− and C_{10}-AuNPs. The initial z values and final z values after 50 ns are labeled above the snapshots. Atoms in the DOPC head groups are omitted for clarity.

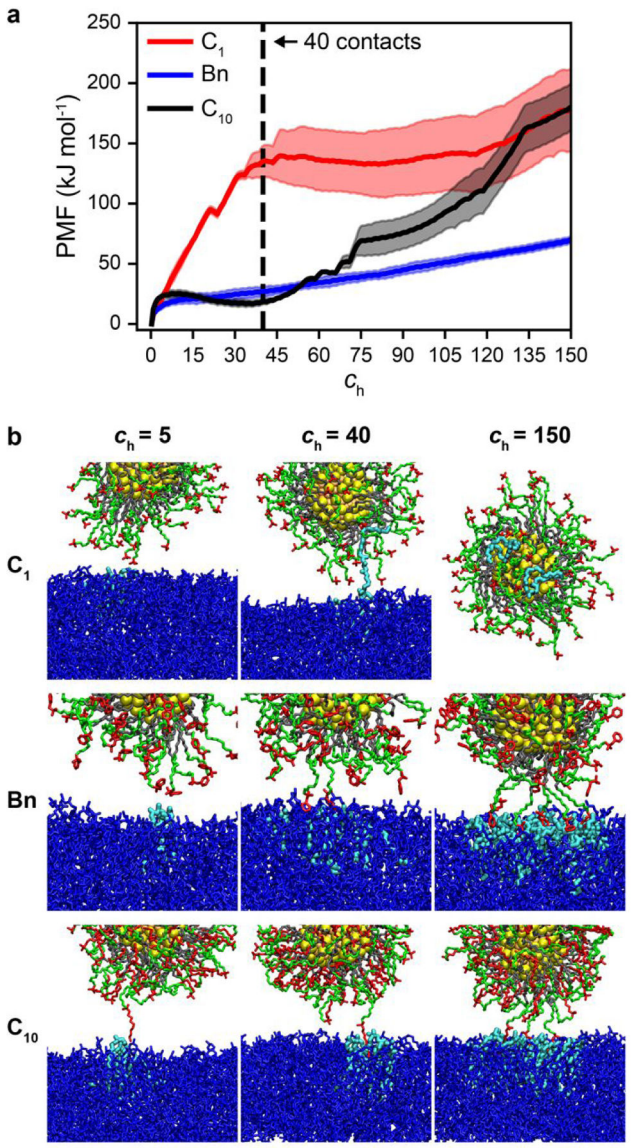

Figure 5.

Free energy as a function of AuNP-bilayer hydrophobic contacts. (a) Potential of mean force (PMF) *versus* the number of hydrophobic contacts (c_h) for C_1−, Bn-, and C_{10}-AuNPs. Error bars are reported as the standard deviation between two 30 ns trajectories for C_1− and C_{10}-AuNPs and two 20 ns trajectories for Bn-AuNP in each umbrella sampling window. (b) Simulation snapshots with c_h = 5, 40, and 150 for C_1−, Bn-, and C_{10}-AuNPs. DOPC lipids that are within 0.35 nm of the ligand atoms are highlighted in cyan.

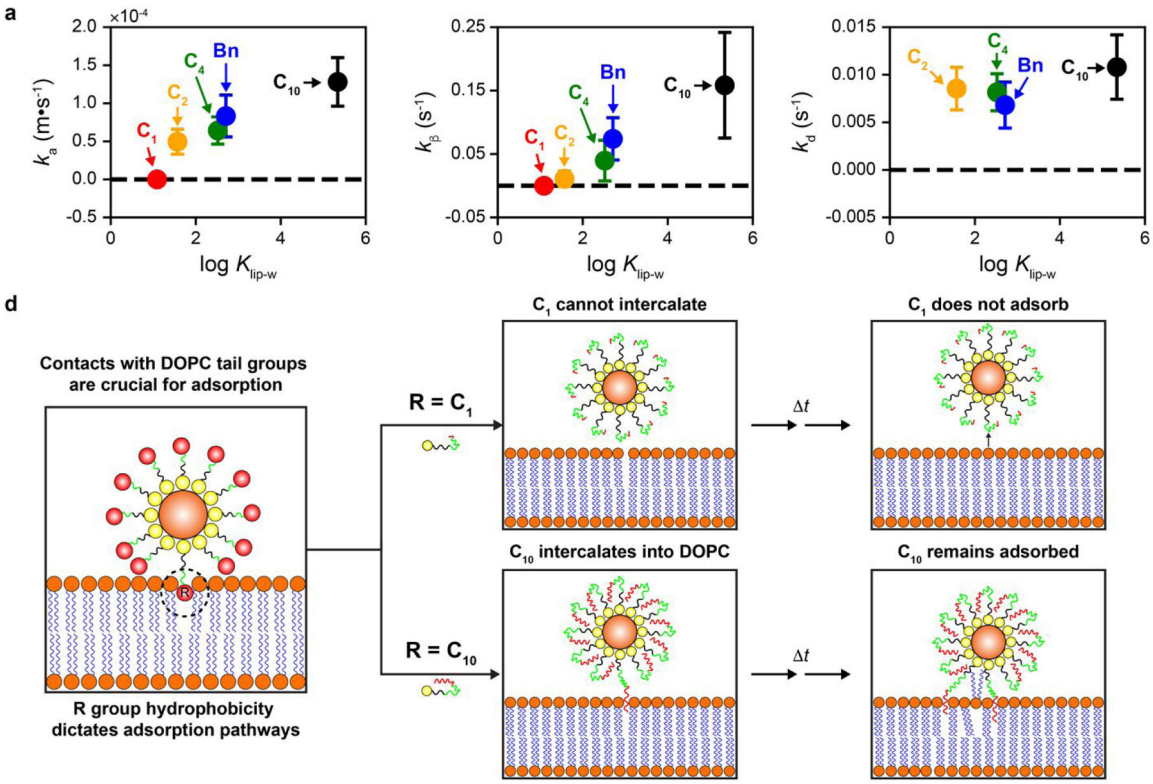

Figure 6.

The role of ligand end group lipophilicity on adsorption to and desorption from phospholipid bilayers. (a) Adsorption rate constant (k_a) calculated from AuNP adsorption with calculated desorption rate constant (k_d) values. (b) Rate constants for conversion to quasi-irreversibly adsorbed state (k_β) calculated from mass at maximum and after rinse. (c) Desorption rate constants (k_d) calculated from AuNP desorption. Error bars represent one standard deviation of four replicate QCM-D measurements. (d) Schematic showing hypothesized mechanism for preferential adsorption of C_{10}-AuNPs compared to C_1-AuNPs. C_{10}-AuNPs have a longer R group, denoted by the red lines. Alkane is shown as black lines and PEG is shown as green lines. The symbol and color for the gold core and lipid bilayer is the same as Figure 1b.